Published in final edited form as:
Nat Neurosci. 2007 September ; 10(9): 1176–1184. doi:10.1038/nn1947.

Adaptive regulation of sparseness by feedforward inhibition

Collins Assisi[1], **Mark Stopfer**[2], **Gilles Laurent**[3], and **Maxim Bazhenov**[1]

[1]The Salk Institute for Biological Studies, 10010 North Torrey Pines Road, La Jolla, California 92037, USA

[2]US National Institutes of Health, National Institute of Child Health and Human Development, 35 Lincoln Drive, MSC 3715, Bethesda, Maryland 20892, USA

[3]California Institute of Technology, 1201 East California Boulevard, Pasadena, California 91125, USA

Abstract

In the mushroom body of insects, odors are represented by very few spikes in a small number of neurons, a highly efficient strategy known as sparse coding. Physiological studies of these neurons have shown that sparseness is maintained across thousand-fold changes in odor concentration. Using a realistic computational model, we propose that sparseness in the olfactory system is regulated by adaptive feedforward inhibition. When odor concentration changes, feedforward inhibition modulates the duration of the temporal window over which the mushroom body neurons may integrate excitatory presynaptic input. This simple adaptive mechanism could maintain the sparseness of sensory representations across wide ranges of stimulus conditions.

Our sensory environment is in near constant flux. Brain sensory systems have evolved the means to adjust their coding properties to adapt to constantly changing signals arising in sensory neurons. Ideally, a coding strategy used by a sensory system should provide efficient representations across the full possible range of stimulation conditions. For the olfactory system, this task involves the encoding of odor intensities, an ability that is critical in many species for survival. Psychophysics studies have shown that, across great ranges of concentrations, odors can be perceived as arising from the same chemical[1,2], and yet, human and animal subjects can distinguish their concentrations as well. Odor representations in the olfactory system have been shown to remain sparse and specific over thousand-fold changes in odor concentration[3], a property that is potentially useful for storing and retrieving memories[4–6]. Given these variations in input, the method by which neural circuits of the olfactory system regulate sensory input to maintain stable odor representations remains a mystery.

Correspondence should be addressed to M.B. (bazhenov@salk.edu).

COMPETING INTERESTS STATEMENT

The authors declare no competing financial interests.

In the antennal lobe, the first relay in the insect olfactory system, odor identity and concentration are encoded by spatiotemporal patterns of activity in populations of projection neurons[4,7,8]. These patterns include the oscillatory synchronization of evolving subsets of projection neurons. This information is then transferred to the mushroom body, a structure analogous to the olfactory cortex. In the locust, recordings made *in vivo* from the Kenyon cells, the principal neurons of the mushroom body, demonstrate remarkable odor specificity[9]. It has been proposed that the intrinsic and synaptic properties of the Kenyon cell circuitry combine to generate relatively brief integration windows in the Kenyon cells, thus causing them to operate as coincidence detectors that are sensitive to their synchronous inputs[9,10]. Notably, recordings made *in vivo* show that the synchrony of the input from the antennal lobe to the mushroom body increases markedly as odor concentration increases[3]. One could predict that this increase in coherence should overwhelm the coincidence detection process, leading to a breakdown in the sparseness of odor representations in the mushroom body as odor concentrations increase. Yet, physiological recordings from Kenyon cells show that their sparse firing is preserved throughout wide ranges in odor concentration[3]. How is sparse coding maintained in the face of this great variance in input intensity?

Feedforward inhibition can effectively regulate the temporal integration properties of neurons[11,12]. In the locust olfactory system, one form of feedforward inhibition consists of competitive interactions between two inputs to Kenyon cells: one input, provided directly by the projection neurons of the antennal lobe, is excitatory, whereas the other, provided indirectly by lateral horn interneurons (LHIs, which themselves are driven by projection neurons)[13], is inhibitory. Feedforward inhibition by LHIs faithfully follows, with a delay, the periodic excitation of Kenyon cells by projection neurons. The alternating cycles of excitation and inhibition create independent and brief temporal windows during which Kenyon cells can sum projection neuron input[9]. This mechanism contributes toward sparsening odor representations in the mushroom body[9]. Here we propose that this mechanism can also maintain representation sparseness across a broad range of stimulus intensities. Using computer simulations we show that changes in projection neuron coherence can modulate the phase of feedforward inhibition to Kenyon cells, and thus adjust their window of integration for projection neuron output. In general, this simple adaptive mechanism may be useful for maintaining sparseness of sensory representations across wide ranges of stimulus conditions.

RESULTS

Encoding odor identity and concentration in the antennal lobe

Odor detection begins when odorant molecules bind to olfactory receptors, initiating a second messenger cascade that leads to the opening of ion channels, the depolarization (usually) of the receptor neuron cell membrane[14] and the generation of action potentials. Because each receptor type responds preferentially to certain odorants, the representation of each odor can be described as a spectrum of activation patterns across the receptor population. As odor concentration increases, less specific receptors become active, leading to broader activity spectra[15–17].

The locust antennal lobe (analogous to the olfactory bulb in mammals) consists of ~830 excitatory projection neurons and 300 inhibitory local neurons, and receives convergent input from ~90,000 olfactory receptor neurons[18] (Fig. 1). In the antennal lobe, receptor neurons appear to synapse onto both projection and local neurons[19]. Local neurons arborize extensively in the antennal lobe, contacting and coordinating large numbers of projection and local neurons[20]. Odor-driven interaction between the excitatory output of receptors and projection neurons, and the inhibitory feedback from local neurons generates a periodic (~20 Hz) projection neuron output[7,21]. To study and simulate this system, we generated a scaled-down model of the antennal lobe consisting of a randomly connected network of 300 projection neurons and 100 local neurons. The connection probability between all pairs of neurons (except projection neuron–projection neuron connections) was set to 0.5; no connections have been observed among projection neurons in the locust (see Methods for a complete description of the model architecture). Odor-evoked oscillatory dynamics could be measured as the mean membrane potential across all projection neurons. As observed *in vivo*[17], the projection neurons whose spikes were phase locked to the oscillatory local field potential (LFP) changed from cycle to cycle.

Using our model, we sought to understand how changes in odor concentration would affect the sparseness of odor representation by downstream areas. We modeled each odor pulse as a continuous and constant (except for low-amplitude additive noise: ~5–10% of the stimulus amplitude) depolarizing input to an odor-specific subset of antennal lobe neurons[22,23]. We emulated the effect of increasing concentration by enlarging the set of activated projection and local neurons (σ, Fig. 2a). Projection neuron oscillatory frequency, as observed *in vivo*[3,7,21], held steady at ~20 Hz across the range of concentrations tested (Fig. 2b). However, the amplitude of the simulated LFP (again, as observed *in vivo*[20]) increased with odor concentration (Fig. 2c), reflecting, primarily, an increase in projection neuron coherence. The amplitude was also augmented by the recruitment of additional projection neurons (Fig. 2a). The mean number of highly active neurons (that is, neurons producing more than 10 spikes per 1-s trial) increased over the range of simulated concentrations (σ = 0.1–0.4), but only by 13%. Further, the number of spikes produced by active neurons decreased from ~25 spikes per simulated trial to ~20 spikes.

To elucidate the role of inhibitory feedback[24] on the concentration-dependent phase locking of projection neurons, we measured the model's total local neuron output to selected projection neurons (the number of Ca^{2+} spikes produced by local neurons presynaptic to a particular projection neuron at each cycle of LFP oscillations over the period between two LFP maxima). This inhibitory input increased, on average, as a function of odor concentration (abscissa, Fig. 2d). As feedback inhibition increased, the timing precision of projection neuron spikes across trials also increased; jitter of projection neuron spikes decreased (ordinate, Fig. 2d). Thus, projection neuron synchrony in our model is adaptively shaped by inhibition and concentration-dependent feedback from local neurons (Fig. 2d). However, the increase of inhibition with odor concentration did not substantially change the frequency of LFP oscillations. We found that an increase in inhibition beyond a certain level only produced an asymptotically small frequency change. Oscillation frequency remained

stabilized at a level determined almost entirely by the decay-time constant of inhibition (for complete analysis see Fig. 2c in ref. 23).

Intracellular recordings from individual projection neurons reveal a variety of odor–elicited firing patterns that are, when seen one projection neuron at a time, poor predictors of the identity or concentration of an odor[3]. Information about identity and concentration, however, can be found when the analysis is carried out over populations of projection neurons[3] in a manner consistent with the way Kenyon cells read projection neuron output[25]. We thus sought to examine the coding of odor concentration across the model's population of projection neurons. We analyzed projection neuron activity as time series of consecutive 300-dimensional vectors ($P_i(j)$, $i = 1,\ldots,300$; $j = 1,\ldots,N$, where N is the total number of consecutive time bins). The space defined by the vectors was reduced by principal component analysis and the population responses to odors were visualized as trajectories projected onto the first three principal components (Fig. 3a). These trajectories, like those calculated for firing patterns recorded *in vivo*[3,26], emerged from baseline (*B*, Fig. 3a), and after a fast transient response, settled into a quasi–steady state. Following odor offset, the projection neuron vectors returned to baseline along a different path. Consistent with experimental recordings[3,26], trajectories corresponding to different odors diverged in the first few cycles of LFP oscillations, and different concentrations of an odor evoked neighboring trajectories (Fig. 3a, right). The quasi–steady state segments of each trajectory were arranged contiguously by concentration, and thus defined odor-specific manifolds in the space of projection neuron activity (Fig. 3a, left). Thus, the output of the model's antennal lobe matches qualitatively the experimental results obtained *in vivo*[3,26].

We further analyzed the relative distances between projection neuron trajectories. The trajectories embedded in a higher dimensional space $[P_i(1) \times P_i(2) \times \ldots \times P_i(N)]$ formed clusters that were odor-identity and concentration specific (Fig. 3b). Across odors, distances between corresponding concentration clusters increased with increasing concentration (Fig. 3b,c, left).

The above results match experimental observations: concentration–dependent increases in intercluster distances were observed in projection neuron recordings with three odor pairs, octanol-hexanol, octanol-geraniol and hexanol-geraniol ($i = 225$ projection neuron vectors, 3 odors × 5 concentrations × 15 trials; Fig. 3c, right). Only when the computed overlap between two simulated odors was extremely high (more than 95% at high concentrations) did inter-concentration cluster distances decrease with concentration.

Decoding olfactory information in the mushroom body

How is this projection neuron spatiotemporal output interpreted by its follower neurons, the Kenyon cells in the mushroom body? Using the total spike output of each one of our model 15,000 Kenyon cells, we created 15,000-dimensional Kenyon cell vectors for each odor presentation. These vectors, constructed for different odors, concentrations and repeated simulated trials, revealed a distributed odor-identity and concentration-dependent organization (Fig. 4a) very much like that seen in experiments; Kenyon cells showed varying degrees of response selectivity, ranging from very selective (activation by a specific odor and concentration) to concentration invariant (activation by all concentrations of a

particular odor) (Fig. 4b). When Kenyon cell firing thresholds were appropriately specified (see below), Kenyon cell responses were sparse, with most of the active (a few hundred out of 15,000) Kenyon cells responding with only 1–3 spikes (Fig. 4c).

Pivotal to the specificity and sparseness of Kenyon cell responses is the underlying architecture of the locust olfactory system, characterized by the wide divergence of connections from projection neurons to Kenyon cells. Each projection neuron arborizes extensively in the mushroom body, on average synapsing onto 50 ± 13% of the Kenyon cells[25]. Conversely, each Kenyon cell reads input from about 50% of the projection neurons[25] (see also[4,27]). This widely divergent connectivity appears to ensure that each Kenyon cell's projection neuron–input vector is maximally different, on average, from those of the other Kenyon cells, provided that their firing thresholds are set appropriately. Kenyon cells can thus be extremely selective and their responses can be sparse, as observed experimentally[3,9]. Of great importance to this sparsening is the control of Kenyon cell integration of projection neuron input defined in part by feedforward inhibition from a small population of interneurons[9] (Fig. 1). Because LHIs are driven by periodic input from projection neurons, their output is also phase-locked, but with a delay defined by the time for conduction and integration by LHIs[9]. Thus, the phase delay between projection neuron and LHI input to Kenyon cells defines the integration window that is available to Kenyon cells at each cycle of the oscillatory projection neuron output[9]. Experiments show that this delay is distributed around a mean of 173° (or about 20 ms)[9].

Experiments[3], reproduced by our simulations here, show that projection neuron coherence increases with odor concentration. Kenyon cells are sensitive to input coincidence in each oscillatory cycle[10]. Therefore, in the absence of any compensatory mechanisms, a concentration-driven increase in projection neuron coherence should lead to an increase in Kenyon cell firing probability[28], compromising the sparseness of odor representations in the mushroom body. However, experiments show that Kenyon cell responses are consistently sparse across thousand-fold changes in concentration[3]. How is this sparseness maintained? Our simulations revealed a plausible mechanism that relies on adaptive regulation of feedforward inhibition by LHIs: as concentration, σ, increases, projection neuron population coherence also increases, but without any systematic changes in the mean timing of projection neuron spikes (Fig. 5a). LHI discharge, however, changes in two major ways. First, LHI coherence increases, leading to stronger phasic inhibitory input to Kenyon cells. Second, LHI mean firing phase advances by up to $\pi/2$ radians, reducing the Kenyon cell integration window, $T(\sigma)$, by up to 10 ms at each oscillation cycle ($dT/d\sigma < 0$) (Fig. 5b).

Why does the LHI spike timing advance without a concurrent change in the peak position of the projection neuron spike distribution? Each LHI receives input from all projection neurons in the antennal lobe, with the width of the projection neuron spike distribution defining the overall strength of input to LHIs. When the distribution of projection neuron spikes was broad (as elicited by low odor concentrations), the sum of projection neuron inputs was near the spiking threshold for many LHIs. Hence, even relatively little variability in the LHI resting potentials (see Methods) produced a substantial effect on the spike times. LHIs receiving barely suprathreshold input produced spikes following a delay, whereas those receiving subthreshold input did not spike at all. Thus, the peak of LHI spiking

became delayed relative to the peak of projection neuron spiking, and the LHI spike distribution was relatively broad. An increase in concentration led to an increase in the coherence of projection neuron spiking (Fig. 5a). In this condition, the LHIs received enough projection neuron input to spike earlier in an LFP cycle. This projection neuron input was substantially higher than what is required by individual LHIs to spike. Therefore, the intrinsic variability in LHI properties (distributed spiking thresholds) did not have a substantial effect on the distribution of spike times. The synchrony of LHI mean firing phase increased nonlinearly with concentration (reflected in a narrow spike distribution), and the peak phase advanced without a systematic shift in the peak timing of projection neuron spikes (Fig. 5b). The peak phase of the projection neuron spike distribution has been shown *in vivo* to be independent of concentration (see Fig. 1C1 and 1C2 in ref. 3 for an analysis of the projection neuron phase distribution; projection neuron raster plots and other examples of raw data are shown in Figs. 2 and 3).

We determined the distribution of action potentials in projection neuron, LHI and Kenyon cell populations (Fig. 6a,b). To examine the change in the balance of inhibitory and excitatory inputs to Kenyon cells for different odor concentrations, we compared spike distributions in Kenyon cells with and without inhibitory input (Fig. 6c,d). Without inhibition, for all odor concentrations, most Kenyon cell spikes occurred after the peak in the LHI spike distribution (Fig. 6c,d, right). An increase in odor concentration increased the coherence and advanced the timing of LHI firing (Fig. 6c, blue line). It also advanced the peak of the Kenyon cell spike distribution (Fig. 6c, dotted black line). However, the overall width of the Kenyon cell distribution remained nearly unchanged (compare Fig. 6d top right and bottom right), a result of the broader distribution of resting potentials in Kenyon cells compared with the distribution of LHI resting potentials. Because almost all LHIs spiked even for moderate odor concentrations, further increases in concentration mainly affected the coherence (and timing) of LHI spikes. In contrast, additional spiking Kenyon cells were recruited across the entire range of odor concentrations; even the highest concentration evoked substantially delayed spiking in Kenyon cells that were near the spiking threshold. *In vivo*, blocking LHI-mediated inhibition by picrotoxin produced a similar effect on Kenyon cell spiking; the number of Kenyon cell spikes increased notably, the distribution of spike times became very broad and the peak of the distribution was delayed from ~$\pi/2$ radians to ~$3\pi/4$ radians[9] (compare this with a change from ~1.3 radians to ~2.5 radians for $\sigma = 0.35$ in the model, Fig. 6c).

When we re-established inhibitory input from LHIs in the model, only a small fraction of Kenyon cell spikes remained. These spikes occurred in the window of integration defined by the mean LHI spike delay (shadowed area in Fig. 6c). Additional Kenyon cell spikes that had occurred later, in the absence of LHI input, were now prevented by LHI-mediated inhibition (Fig. 6d, left; note *y*-axis scale change for Kenyon cell distribution). Because the mean firing phase of LHIs advanced for higher odor concentrations, the mean number of Kenyon cell spikes in the model with LHI inhibition remained nearly constant across the range of concentrations. In contrast, in the model without LHI inhibition, the height of the Kenyon cell spike distribution increased markedly with an increase in concentration. (Fig. 6d, right).

We can see, qualitatively at least, how projection neuron population output changes are compensated for by changes in the strength and timing of LHI output. We then analyzed the effects of this regulation of LHI output on Kenyon cells. We adjusted our model to selectively eliminate the modulation of LHI phase by introducing an artificial delay $\Delta(\sigma)$, a function of the concentration ($d\Delta/d\sigma > 0$), into the LHI input to Kenyon cells (Fig. 7a). In this condition, projection neuron output coherence increased with concentration, and the feedforward inhibition by LHIs retained all of its attendant characteristics, except for the aforementioned phase advance (the new Kenyon cell integration window, $T_1 = T(\sigma)+\Delta(\sigma)$, remained fixed: $dT_1/d\sigma = 0$). As predicted, the effect on Kenyon cells was substantial, causing explosive Kenyon cell activation for $\sigma > 0.25$ (Fig. 7b). For $\sigma = 0.4$ ($\sigma = 0.35$) the total number of Kenyon cell spikes was ~35,000 (~17,500) with 13,080 (9,172) out of 15,000 Kenyon cells spiking at least once. By contrast, allowing feedforward inhibition from LHIs to adapt freely to projection neuron coherence (Fig. 7b; that is, to advance as projection neuron coherence increased) led to very tight regulation of Kenyon cell output, and maintained Kenyon cell sparseness over a wide range of concentrations. The introduction of additional fixed delays, Δ_0, but keeping the integration window adaptive ($T_1(\sigma) = T(\sigma)+\Delta_0$, $dT_1/d\sigma < 0$), kept Kenyon cell activity at experimental levels of sparseness for Δ_0 between 0.0 ms and ~2 ms. Additional delays beyond ~3 ms led to unrealistic Kenyon cell activation. Notably, maximum regulation was observed when no additional delay (0.0 ms) was introduced, when the system adapted autonomously to input coherence.

Adaptive feedforward inhibition in a minimal circuit

We investigated the principle underlying this self-regulation in a reduced model that consisted of a pair of neurons coupled by an inhibitory synapse (Fig. 8). Spike trains with normally distributed spike-arrival times, emulating input from the antennal lobe over a single oscillation cycle, were delivered to both neurons, with the model Kenyon cell receiving only a fraction of the drive to the LHI (Fig. 8a). We systematically manipulated the width of this spike-arrival–time distribution (Fig. 8c, top panel) to simulate the changes in projection neuron coherence caused by changing odor concentration (single trials, Fig. 8c, lower 3 panels; measured as the probability over 200 independent trials, Fig. 8b, top panel). Increases in input coherence (decreased s.d.) increased LHI firing probability (Fig. 8b, top; Fig. 8c, second panel). This increase in LHI response probability was accompanied by a decrease in the mean delay to an LHI spike (Fig. 8c, bottom; see also Fig. 8b, second panel for a single trial); it is this delay that defines the Kenyon cell integration window (blue shaded area, Fig. 8b, second panel). A notable feature of the Kenyon cell response in the presence of feedforward inhibition (Fig. 8b, top; Fig. 8c, third panel) is its consistently low firing probability over the range of input coherence tested. In this minimal model, the regulation of Kenyon cell firing probability, a prerequisite for sparseness in the full-scale model network, was lost when feedforward inhibition was eliminated (Fig. 8b, top; Fig. 8c, bottom). In the absence of inhibition, most of the Kenyon cell spikes occurred outside of the window of integration defined by the mean LHI spike delay (the dotted black line in Fig. 8b, bottom panel, lies outside the shaded area). Two key factors involved in the regulation of Kenyon cell spiking by feedforward inhibition are thus revealed. First, an increase in input coherence necessarily advances the mean firing time of the LHIs. Second, potential (but

normally suppressed) Kenyon cell spikes (that is, spikes permitted by the absence of feedforward inhibition) must be distributed such that a substantial proportion of them would occur outside of the normal window of integration. This prediction is consistent with experiments. Blocking phasic inhibition of Kenyon cells both increased their response probability and eliminated their phase locking to the LFP[9], even though projection neuron drive to them remained phasic and oscillatory. More generally, we note that these two factors may be easily accomplished in any network where the input to the neurons requiring regulation (such as Kenyon cells) comes from a population of inhibitory inter-neurons (such as LHIs) with different levels of excitability (instantiated here by a random distribution of resting potentials).

DISCUSSION

The progression of olfactory information from olfactory receptors to higher brain structures includes multiple levels of processing and involves complex strategies for the efficient encoding of information. In the insect antennal lobe, input from olfactory receptors triggers dynamic spatiotemporal patterns of neuronal activity including oscillatory synchronization to encode the identity and concentration of odors[3,4,7,8]. Although the fine temporal structure in these patterns may contribute relatively little to coding and decoding in simple olfactory tasks such as when discriminating ensembles of receptors that do not significantly overlap with one another (activated, perhaps, by odorants with chemically distinct structures), fine temporal features appear to become critical when discrimination tasks are more challenging, such as when activated ensembles of olfactory receptors substantially overlap[29]. Such overlap is elicited by odors that are chemically similar, and by different concentrations of the same odor[3].

Recordings made *in vivo* from the locust antennal lobe revealed that changes in odor concentration led to a complex and nonlinear evolution in the response patterns of projection neurons[3]. An analysis of large populations of projection neurons showed that an important invariance emerged from the antennal lobe dynamics: different concentrations of the same odors induced responses that formed an odorant-specific manifold in a high-dimensional space of all projection neuron responses. This concentration-dependent structure of the antennal lobe response patterns resulted, in part, from marked increases in the coherence of projection neurons at higher odor concentrations[3]. Here, with simulations in a realistic antennal lobe model, we found that, when odor concentrations were higher, a larger fraction of the inhibitory local neurons produced spikes during odor stimulation. In turn, these spikes increased the precision of projection neuron spiking. Changes in the activity of groups of local neurons over the odor duration[23] have been proposed as a mechanism for transient projection neuron synchronization[7,8]. Here we found that the same mechanism can modulate the synchronization properties of projection neuron responses across a range of odor concentrations. Our model's simulated antennal lobe network preserves the salient properties seen in the experiment, including odor and concentration-based clustering, while maintaining local field oscillations at approximately 20 Hz. When odor representations at each time point were considered as instantaneous vectors of activity across the whole projection neuron population in the model, the vectors corresponding to different odors

diverged in the first few cycles of the local field oscillations, whereas different concentrations of a particular odor formed neighboring trajectories.

In insects, odor information processed in the antennal lobe is transferred to the mushroom body, a structure analogous to the olfactory cortex, and one important for memory formation[4–6]. Implementing both antennal lobe and mushroom body circuitry in our model, we found that a manifold formed by projection neuron responses for different concentrations of a given odor is mapped into a higher-order manifold in the Kenyon cell activity space. Because of the very large number of Kenyon cells, however, mushroom body responses for different odor concentrations formed well-separated clusters with little or no overlap, even for close (and highly overlapping at the level of the input to the antennal lobe) odor concentrations. Therefore, the odor concentration–specific structure of the neuronal responses in the antennal lobe is transmitted to the mushroom body; this structure allows for the use of potentially simple and efficient strategies to discriminate and categorize different odors and different odor concentrations. Maintaining the sparseness of Kenyon cell responses across the broad range of odor concentrations is essential to the efficiency of this encoding process. Indeed, recordings made *in vivo* from the mushroom body demonstrate that typically only a few Kenyon cells from a recorded population of neurons respond reliably when an odor is presented[9]. Different odors, and different concentrations of odors, can induce responses in different Kenyon cells[3]. Such response specificity in the mushroom body was proposed to depend on the coincidence detection properties of the Kenyon cells[9,10].

Coincidence detection offers a number of advantages for encoding sensory information over integration, including greater stability against input noise[28,30] and greater ability to discriminate among related input vectors[9]. However, encoding by coincidence detection is necessarily more sensitive to global changes in the temporal structure of the input. To achieve sparse and selective representations, coincidence detectors must operate near a critical point that allows relatively few synchronous inputs to elicit a spike in the given integration window. However, assuming a continuous distribution of coherence across inputs, coincidence detection may be easily saturated by even a moderate increase in overall input synchrony. An example of this phenomenon is provided by olfaction. An increase in odor concentration leads to such an increase in coherence, therefore destabilizing the fine balance between the properties of the input and intrinsic characteristics of Kenyon cell circuitry. This would, in contradiction to the experimental data, lead to a loss in the sparseness of representation in the mushroom body.

Our model, which is constrained by well-characterized features of the locust olfactory system, shows that stability against global changes in the temporal structure of the input can be achieved by an adaptive, dynamic integration window that is itself dependent on the stimulus. Delayed, discrete feedforward inhibition from the same input that provides excitation, as found here, can endow coincidence detectors with the requisite properties. As odor concentration increased, it advanced the timing of the peak of the inhibitory input, thus effectively reducing the integration window of the Kenyon cells. Therefore, the necessary balance between the input properties (degree of projection neurons coherence) and the properties of the Kenyon cells circuitry (size of the integration window) is maintained

automatically through a range of stimulation intensities. Earlier studies have implicated feedforward inhibition in regulating the temporal integration of inputs[11,12]. However, the subtle adaptive nature of feedforward inhibition, essential for maintaining sparseness of odor representations, has thus far been overlooked.

It has been proposed before that stimulus-dependent phase shifts between neurons could encode information[31]. In contrast, we propose that such shifts are not encoding variables; instead, they have a structural role in maintaining response density across a wide range of input conditions. The existence of comparable feedforward inhibitory pathways in a number of neural circuits, including hippocampus[11,32], cerebellum[12,27], lateral geniculate nucleus[33] and sensory circuits sensitive to the precise timing of excitatory input[6,34], suggests the potentially widespread applicability of the mechanism described here.

METHODS

Antennal lobe model

The antennal lobe model included 300 projection neurons and 100 local neurons, and is based on a previous model[22,23]. Individual projection and local neurons were modeled by a single compartment that included voltage- and Ca^{2+}-dependent currents described by Hodgkin–Huxley kinetics[23]. In the model, isolated projection neurons showed overshooting Na^{+} spikes at a fixed frequency throughout constant depolarizing stimulation. Local neurons, in contrast, fired low-amplitude Ca^{2+} spikes and demonstrated spike-frequency adaptation caused by Ca^{2+}-dependent potassium currents. Fast GABA (local neuron–projection neuron and local neuron–local neuron connections) and nicotinic cholinergic synaptic currents (projection neuron–local neuron connections) were modeled by first-order activation schemes[35]. Slow GABAergic synapses (local neuron–projection neuron connections) were added to account for slow temporal patterns in network activity[20,36]. In the model, the slow inhibitory receptors could only be activated by a long train of local neuron Ca^{2+} spikes at relatively high frequencies, and the maximal conductance was set low compared with the fast GABA conductance so that the slow dynamics did not affect the 20-Hz oscillations. Maximal conductances denoting the total excitation and inhibition received by a given cell were set to G_{ACh} (projection neuron–local neuron) =0.5 μS, G_{GABA_fast} (local neuron–projection neuron) = 0.4 μS, G_{GABA_slow} (local neuron–projection neuron) = 0.025 μS, and $G_{GABAfast}$ (local neuron–local neuron) = 0.2 μS. All interconnections in the antennal lobe model were random, with a probability of 0.5. The equations for all intrinsic and synaptic currents are given in[22,23].

Kenyon cell and LHI model

To study the odor representations in the mushroom body, we must take into account[25] the vast divergence of connections from the antennal lobe to the mushroom body. This task necessitates a large number of model neurons and large computational resources. To circumvent this, we generated a reduced and computationally efficient neuronal model for both Kenyon cells and LHIs[37,38]. This model, despite its low dimensionality, produces a rich repertoire of dynamics and has been shown to mimic the dynamics of Hodgkin-Huxley–type neurons, both at the single–cell level and in the context of network dynamics[37,38]. Kenyon

cells (15,000 cells) and LHIs (100 cells) were modeled as regular spiking cells (equations 1 and 2 in ref. 38) with synaptic interactions according to equation (5) in ref. 38. The model parameter σ (equation 1 in ref. 38) affects the resting potential (and therefore, the spiking threshold) of LHIs and Kenyon cells. For the population of LHIs, σ was picked randomly from a uniform distribution over the interval (0.03, 0.04) to provide some variation in the spike timing across all LHIs. Given the small number of LHIs (n = 100), we chose a uniform distribution as an unbiased estimate of the LHI resting potentials. The value of σ for Kenyon cells (n = 15,000) was picked from a Gaussian distribution with a mean of 0.03 and an s.d. of 0.01, ensuring a broader distribution of Kenyon cell resting potentials. Preliminary simulations indicated that our specific choice of distribution was not critical to the conclusions of our model. The minimum value of σ for Kenyon cells was 0.001 and the maximum was 0.06. Maximal conductances (in dimensionless units, see ref. 38) denoting the total excitation and inhibition received by a given cell were set to G_{ACh}(projection neuron–Kenyon cell) = 0.0008, G_{ACh}(projection neuron–LHI) = 0.0015, and G_{GABA_fast} (LHI–Kenyon cell) = 0.005. This choice of spiking thresholds and the strength of synaptic input from the antennal lobe were set such that a minimal (nonzero) response could be elicited from Kenyon cells for the lowest concentration tested, and to achieve substantial LHI firing even for moderate odor concentrations.

Stimulation

The intensity (amplitude) of the stimulus to projection neurons and local neurons followed a Gaussian distribution truncated at 0.1 to avoid stimulating all projection neurons. We randomly determined which projection and local neurons received input with a particular intensity. The proportion of local neurons receiving non–zero input was approximately one third that of projection neurons receiving nonzero input. The temporal variation of the stimulus was modeled by a current pulse with a rise-time constant of 100 ms and a decay-time constant of 200 ms[22,23,39]. The current used for each pulse was calculated as the total synaptic current produced by N Poisson-distributed spike trains (each with average spike rate μ) arriving at N-independent excitatory synapses. Each glomerulus in the locust antennal lobe is thought to receive between 100 and 200 axons from olfactory receptors neurons[40]. In our simulations N was set to 200 and μ to 100 Hz to match the membrane potential fluctuations recorded in postsynaptic projection neurons *in vivo* (for example, Fig. 2 in ref. 41).

Reduced two-cell network

Both the LHI and Kenyon cell in the two–cell network were modeled using the same equations[37,38] as in the full network. The Kenyon cell and LHI were connected by an inhibitory synapse. Both received external input through N = 100 excitatory synapses. All N synapses were connected to the LHI and N/3 randomly selected synapses were connected to the Kenyon cell. The spike times in each synapse were independent and taken from a normal distribution with s.d. varying between 1 and 22 ms. The stimulation was repeated independently 200 times.

Analysis

We first generated a time series consisting of the spike counts over 50-ms bins for all projection neurons. The resulting 300-dimensional time series (ten odor presentations, two odors and five concentrations) were concatenated before computing the principal components over the entire data set. We show 300-dimensional time series projected onto the first three principal components (~65% variance) in Figure 3a. Each point in a trajectory corresponds to the number of spikes in each of the 300 projection neurons in a 50-ms bin; the entire 3-s trajectory consists of 60 such points. The complete trajectories were embedded in a higher-dimensional space (300 projection neurons × 60 time points) where each vector represents the spatiotemporal pattern of projection neuron activity over the duration of an odor presentation (Fig. 3b). The 300 × 60–dimensional vectors corresponding to all the conditions were concatenated before calculating the principal components (Fig. 3b was obtained by projecting these high-dimensional vectors onto the first three principal components, ~65% of variance). The phase values used to construct the distributions in Figures 5, 6 and 7 were generated using the projection neuron LFP as a reference. The oscillatory LFP was first filtered (5–25 Hz) and the instantaneous phase was calculated using a Hilbert transform.

Experimental data

Young adult locusts (n = 54, *Schistocera americana*) were immobilized with one antenna intact and fixed in place. The brain was exposed, desheathed and bathed in locust saline as previously described[42,43]. LFPs were recorded either using saline-filled blunt glass micropipettes (tip ~10 μm, ~10 MΩ) with a direct current amplifier (NPI, Adams-List) or with custom wire tetrodes. Intracellular and extracellular recordings from projection neurons were made as described[3]. For experiments with extracellular recordings, octanol, hexanol and geraniol were mineral oil–dilution standardized by vapor pressure in accordance with Raoult's law, and then serially diluted to yield strengths of 0.001, 0.01, 0.05, 0.1 or 1 × that of the standard.

Acknowledgments

This work was supported by grants from the US National Institute of Deafness and other Communication Disorders (C.A., G.L. and M.B.), the National Science Foundation (G.L.) and a US National Institute of Child Health and Human Development intramural award (M.S.).

References

1. Gross-Isseroff R, Lancet D. Concentration-dependent changes of perceived odor quality. Chem Senses. 1988; 13:191–204.
2. Bhagavan S, Smith BH. Olfactory conditioning in the honey bee, *Apis mellifera*: effects of odor intensity. Physiol Behav. 1997; 61:107–117. [PubMed: 8976540]
3. Stopfer M, Jayaraman V, Laurent G. Intensity versus identity coding in an olfactory system. Neuron. 2003; 39:991–1004. [PubMed: 12971898]
4. Laurent G. Olfactory network dynamics and the coding of multidimensional signals. Nat Rev Neurosci. 2002; 3:884–895. [PubMed: 12415296]
5. Kanerva, P. Sparse Distributed Memory. Bradford Books; Boston: 1988.
6. Olshausen BA, Field DJ. Sparse coding of sensory inputs. Curr Opin Neurobiol. 2004; 14:481–487. [PubMed: 15321069]

7. Wehr M, Laurent G. Odour encoding by temporal sequences of firing in oscillating neural assemblies. Nature. 1996; 384:162–166. [PubMed: 8906790]
8. Laurent G, Wehr M, Davidowitz H. Temporal representations of odors in an olfactory network. J Neurosci. 1996; 16:3837–3847. [PubMed: 8656278]
9. Perez-Orive J, et al. Oscillations and sparsening of odor representations in the mushroom body. Science. 2002; 297:359–365. [PubMed: 12130775]
10. Perez-Orive J, Bazhenov M, Laurent G. Intrinsic and circuit properties favor coincidence detection for decoding oscillatory input. J Neurosci. 2004; 24:6037–6047. [PubMed: 15229251]
11. Pouille F, Scanziani M. Enforcement of temporal fidelity in pyramidal cells by somatic feedforward inhibition. Science. 2001; 293:1159–1163. [PubMed: 11498596]
12. Mittmann W, Koch U, Hausser M. Feedforward inhibition shapes the spike output of cerebellar Purkinje cells. J Physiol (Lond). 2005; 563:369–378. [PubMed: 15613376]
13. Anton, S.; Homberg, U. Antennal lobe structure. In: Hansson, BS., editor. Insect Olfaction. Springer; Berlin: 1999.
14. Matthews HR, Reisert J. Calcium, the two-faced messenger of olfactory transduction and adaptation. Curr Opin Neurobiol. 2003; 13:469–475. [PubMed: 12965295]
15. Anderson P, Hansson BS, Löfqvist J. Plant-odour–specific receptor neurones on the antennae of female and male Spodoptera littoralis. Physiol Entomol. 1995; 20:189–198.
16. Hallem EA, Carlson JR. Coding of odors by a receptor repertoire. Cell. 2006; 125:143–160. [PubMed: 16615896]
17. Hallem EA, Ho MG, Carlson JR. The molecular basis of odor coding in the *Drosophila* antenna. Cell. 2004; 117:965–979. [PubMed: 15210116]
18. Ernst KD, Boeckh J, Boeckh V. A neuroanatomical study on the organization of the central antennal pathways in insects. Cell Tissue Res. 1977; 176:285–306. [PubMed: 832298]
19. MacLeod K, Backer A, Laurent G. Who reads temporal information contained across synchronized and oscillatory spike trains? Nature. 1998; 395:693–698. [PubMed: 9790189]
20. MacLeod K, Laurent G. Distinct mechanisms for synchronization and temporal patterning of odor-encoding neural assemblies. Science. 1996; 274:976–979. [PubMed: 8875938]
21. Laurent G, Davidowitz H. Encoding of olfactory information with oscillating neural assemblies. Science. 1994; 265:1872–1875. [PubMed: 17797226]
22. Bazhenov M, et al. Model of cellular and network mechanisms for odor-evoked temporal patterning in the locust antennal lobe. Neuron. 2001; 30:569–581. [PubMed: 11395015]
23. Bazhenov M, et al. Model of transient oscillatory synchronization in the locust antennal lobe. Neuron. 2001; 30:553–567. [PubMed: 11395014]
24. Margrie TW, Sakmann B, Urban NN. Action potential propagation in mitral cell lateral dendrites is decremental and controls recurrent and lateral inhibition in the mammalian olfactory bulb. Proc Natl Acad Sci USA. 2001; 98:319–324. [PubMed: 11120888]
25. Jortner RA, Farivar SS, Laurent G. A simple connectivity scheme for sparse coding in an olfactory system. J Neurosci. 2007; 27:1659–1669. [PubMed: 17301174]
26. Mazor O, Laurent G. Transient dynamics versus fixed points in odor representations by locust antennal lobe projection neurons. Neuron. 2005; 48:661–673. [PubMed: 16301181]
27. Marr D. A theory of cerebellar cortex. J Physiol (Lond). 1969; 202:437–470. [PubMed: 5784296]
28. Salinas E, Sejnowski TJ. Impact of correlated synaptic input on output firing rate and variability in simple neuronal models. J Neurosci. 2000; 20:6193–6209. [PubMed: 10934269]
29. Stopfer M, Bhagavan S, Smith BH, Laurent G. Impaired odour discrimination on desynchronization of odour-encoding neural assemblies. Nature. 1997; 390:70–74. [PubMed: 9363891]
30. Konig P, Engel AK, Singer W. Integrator or coincidence detector? The role of the cortical neuron revisited. Trends Neurosci. 1996; 19:130–137. [PubMed: 8658595]
31. Hopfield JJ. Pattern recognition computation using action potential timing for stimulus representation. Nature. 1995; 376:33–36. [PubMed: 7596429]
32. Buzsaki G. Feedforward inhibition in the hippocampal formation. Prog Neurobiol. 1984; 22:131–153. [PubMed: 6433403]

33. Blitz DM, Regehr WG. Timing and specificity of feed-forward inhibition within the LGN. Neuron. 2005; 45:917–928. [PubMed: 15797552]
34. Sun QQ, Huguenard JR, Prince DA. Barrel cortex microcircuits: thalamocortical feedforward inhibition in spiny stellate cells is mediated by a small number of fast-spiking interneurons. J Neurosci. 2006; 26:1219–1230. [PubMed: 16436609]
35. Destexhe A, Mainen ZF, Sejnowski TJ. Synthesis of models for excitable membranes, synaptic transmission and neuromodulation using a common kinetic formalism. J Comput Neurosci. 1994; 1:195–230. [PubMed: 8792231]
36. Wilson RI, Laurent G. Role of GABAergic inhibition in shaping odor-evoked spatiotemporal patterns in the *Drosophila* antennal lobe. J Neurosci. 2005; 25:9069–9079. [PubMed: 16207866]
37. Rulkov NF, Timofeev I, Bazhenov M. Oscillations in large-scale cortical networks: map-based model. J Comput Neurosci. 2004; 17:203–223. [PubMed: 15306740]
38. Bazhenov M, Rulkov NF, Fellous JM, Timofeev I. Role of network dynamics in shaping spike-timing reliability. Phys Rev E. 2005; 72:041903.
39. Bazhenov M, Stopfer M, Sejnowski TJ, Laurent G. Fast odor learning improves reliability of odor responses in the locust antennal lobe. Neuron. 2005; 46:483–492. [PubMed: 15882647]
40. Laurent G. Dynamical representation of odors by oscillating and evolving neural assemblies. Trends Neurosci. 1996; 19:489–496. [PubMed: 8931275]
41. Wehr M, Laurent G. Relationship between afferent and central temporal patterns in the locust olfactory system. J Neurosci. 1999; 19:381–390. [PubMed: 9870967]
42. Laurent G, Naraghi M. Odorant-induced oscillations in the mushroom bodies of the locust. J Neurosci. 1994; 14:2993–3004. [PubMed: 8182454]
43. Stopfer M, Laurent G. Short-term memory in olfactory network dynamics. Nature. 1999; 402:664–668. [PubMed: 10604472]

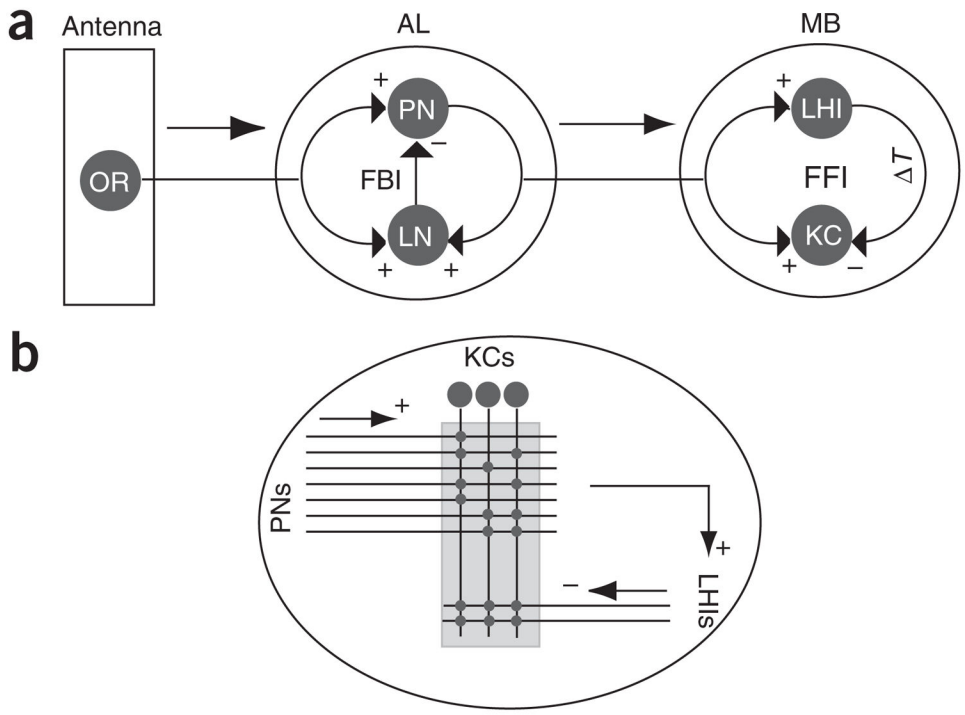

Figure 1.

Network structure. (**a**) The excitatory projection neurons (PN = 300) and inhibitory local interneurons (LNs = 100) receive input from olfactory receptor (OR) neurons. The PN-LN and LN-LN connection probability was set to 0.5. PNs receive feedback inhibition (FBI) from LNs. No connections were implemented between PNs. The LHIs (100) provide delayed (ΔT) feedforward inhibition (FFI) to the Kenyon cells (KCs = 15,000). (**b**) A detailed view of projections from PNs to the mushroom body (MB). The PNs project to the mushroom body along two pathways: a monosynaptic direct connection and a disynaptic pathway via the LHIs. The PN→LHI and the LHI→KC connections are all to all. Approximately 100 PNs synapse onto each KC.

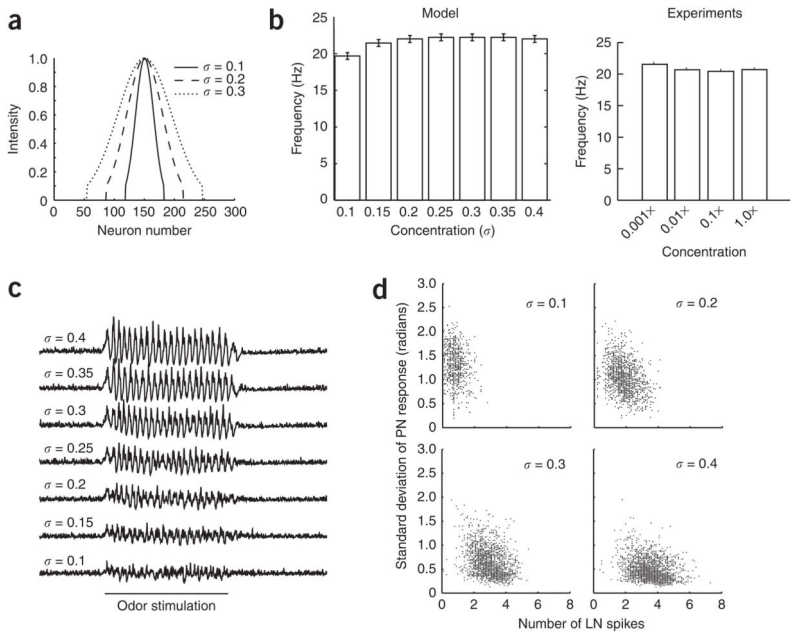

Figure 2.

Oscillatory dynamics of antennal lobe neurons for different odor concentrations. (**a**) For a particular odor, the input from the olfactory receptor neuron array is maximal to some projection neurons and progressively less to others. An increase in concentration is instantiated in the model by recruiting additional projection neurons. A quantitative measure of the concentration is the s.d., σ, of the input Gaussians. Three different concentrations used in the simulations are shown. Different odors may be simulated by shifting these curves along the abscissa, with the degree of overlap between Gaussians indicating the similarity between modeled odors. (**b**) LFP oscillation frequency for different concentrations. Left, mean frequency of the membrane potential of 300 projection neurons as a function of concentration ranging from $\sigma = 0.1–0.4$. Right, frequency of the LFP at four concentrations. An increase in concentration does not cause large variations in the frequency of the LFP, which remains around 20 Hz. (**c**) The membrane potential averaged across 300 projection neurons for different modeled concentrations. The amplitude of the oscillations increased with concentration. The horizontal line shows the time over which the stimulus was presented (duration = 1 s). (**d**) Mean number of spikes in all presynaptic local neurons versus the s.d. in the spike timing of their postsynaptic projection neurons across trials. The s.d. is computed in terms of the phase of the oscillatory LFP at which a projection neuron fires a spike. Increasing concentration led to an increase in the number of presynaptic local neuron spikes and a corresponding increase in the reliability of projection neuron spike phase across trials.

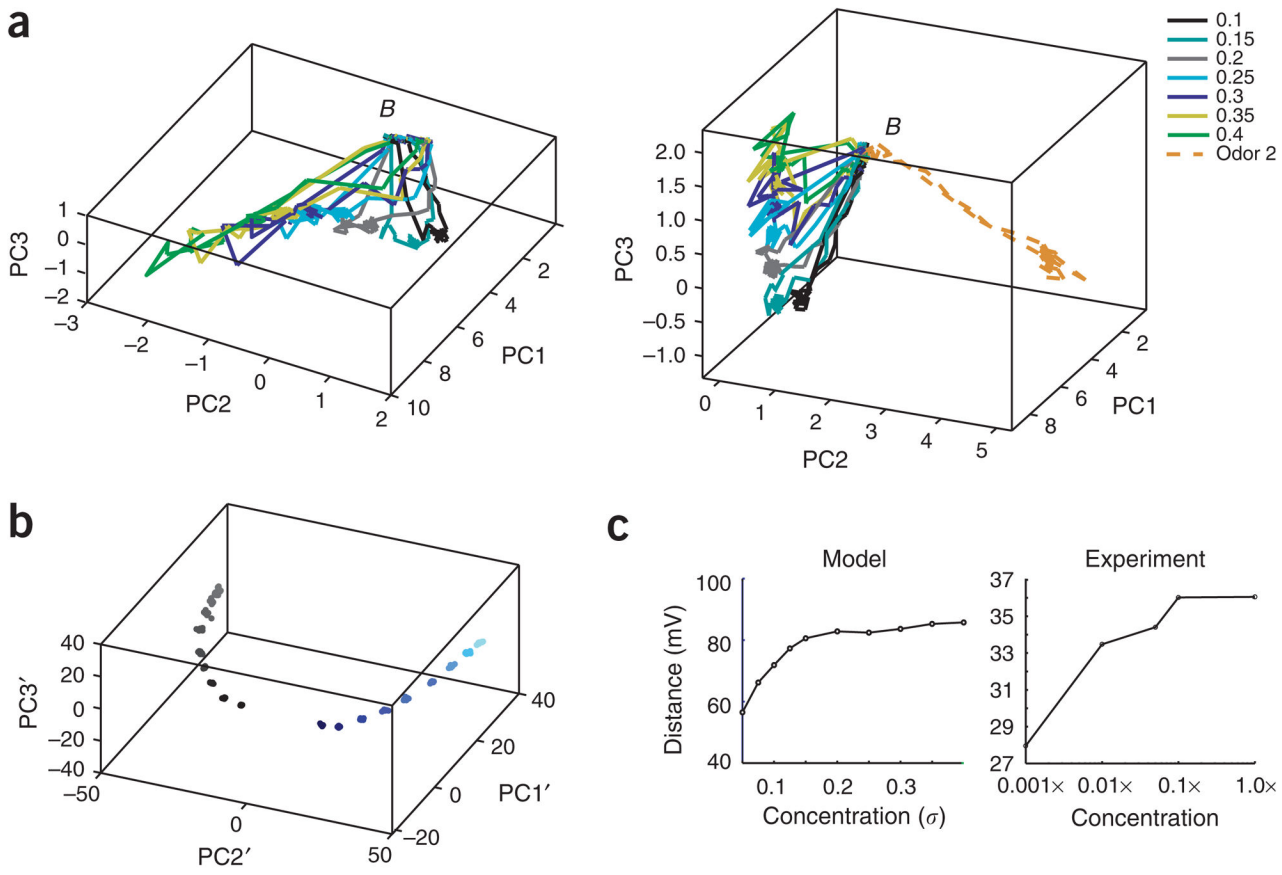

Figure 3.

Collective dynamics of neurons in the modeled antennal lobe. (**a**) Visualization of the spatiotemporal dynamics of the 300 model projection neurons projected onto the first three principal components (mean over ten odor presentations, binned using 50-ms windows). Each trajectory covers 3 s, with the stimulus presented over 1 s. The trajectories originate from baseline (*B*). Different concentrations (σ) of the same odor (shown in different colors) evolved along neighboring trajectories (left), whereas different odors evolved along divergent trajectories (right). (**b**) Clustering of the spatiotemporal response patterns of the 300 model projection neurons for two odors across a range of six concentrations. Here, each trajectory shown in **a** is treated as a single point in a higher-dimensional space; each point corresponds to the response of the projection neuron ensemble to an odor presentation. The points clustered in an odor- (color) and concentration-dependent (shade) manner. The spatiotemporal response of the projection neuron ensemble diverged as a function of increasing concentration. The high-dimensional spatiotemporal patterns are projected onto the first three principal components for visualization. Dark color, low concentrations; light color, high concentrations. (**c**) The Euclidean distance between odor clusters as a function of odor concentration. Left, in the model, the distance increased for concentrations from 0.05 to ~0.25 and remained nearly constant for higher concentrations (σ = 0.25–0.4). Right, experimental data showing an increase in the distance between odor clusters (averaged for three odor pairs) from 10^{-3} to 10^{-1}, followed by saturation between 10^{-1} and 1.

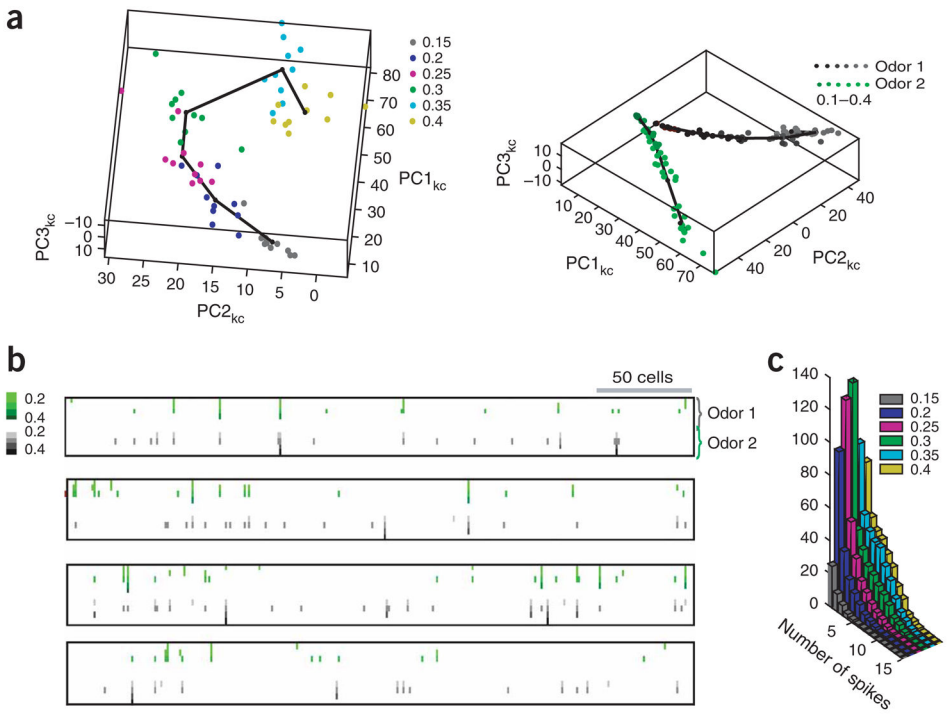

Figure 4.

Collective dynamics of neurons in the modeled mushroom body. (**a**) Visualization of the model KC activity projected onto the first three principal components. Left, KC activity was computed by adding the number of spikes produced by each of 15,000 KCs over the stimulus duration to obtain a 15,000-dimensional vector. Each point corresponds to one trial of an odor presentation. The line joins the means of different concentration (different colors) clusters. Right, KC activity clustered along different concentration manifolds for dissimilar odors. (**b**) Diversity of KC responses to odor concentrations. Each plotted point represents an active KC (cells that spike in more than 50% of the trials). Individual KCs showed varying degrees of selectivity to different odor concentrations (dark color, low concentrations; light color, high concentrations; different colors correspond to different odors). Some cells spiked reliably for a wide range of concentrations, whereas others were responsive to specific odor-concentration pairs. Each panel consists of 300 randomly selected KCs. (**c**) Frequency distribution of KC response intensity (total number of spikes elicited by a 1-s odor presentation). Most cells responded with 1–3 spikes.

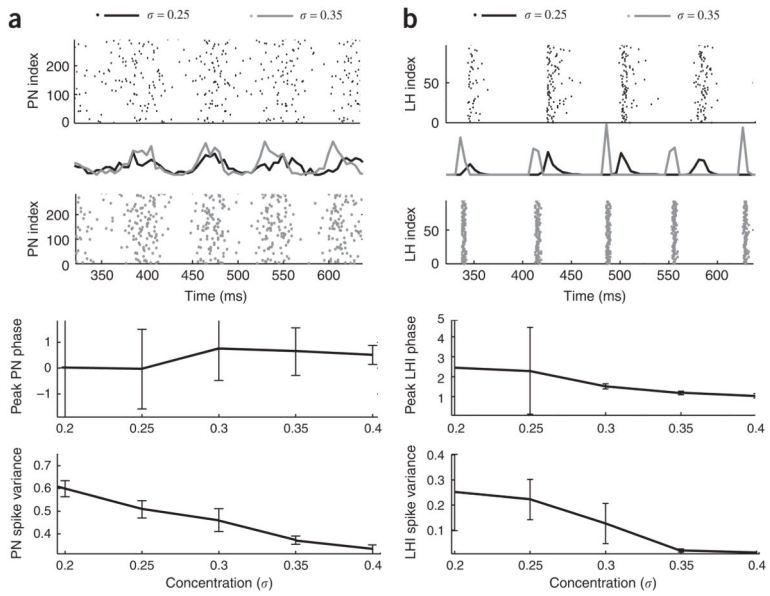

Figure 5.

PN and LHI responses for different odor concentrations. (**a**,**b**) Top, the activity histogram and spike raster of PNs (**a**) and LHIs (**b**), shown for two concentrations. The timing of the peak activity of PNs did not show a clear dependence on concentration. The timing of peak LHI activity advanced for higher concentrations and LHI spiking became more coherent. The amplitude of LHI activity histograms (top) is rescaled. Bottom, the peak phase and the variance in the phase distribution for each concentration are shown for PNs (**a**) and LHIs (**b**). The peak PN phase did not advance systematically as a function of increasing concentration; variance of the PN phase, however, decreased consistently with increasing concentration. Solid lines show average network activity.

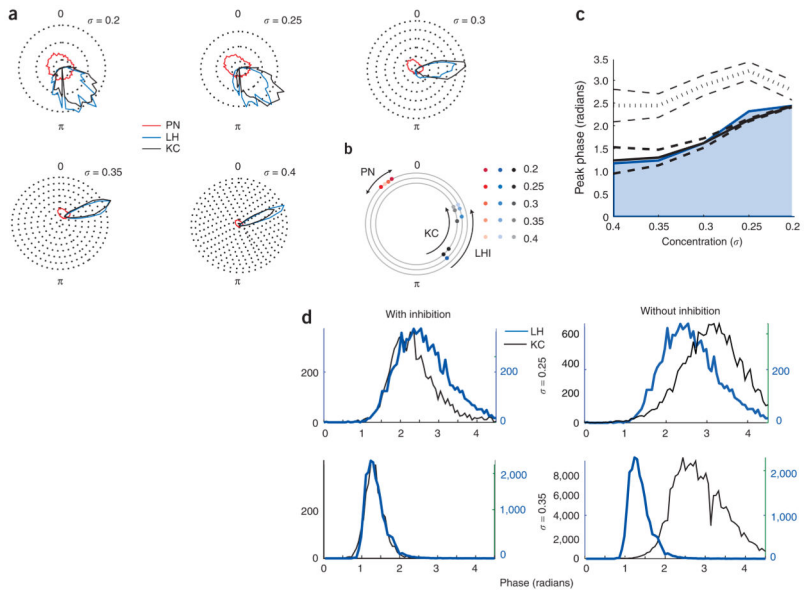

Figure 6.

Effect of adaptive feedforward inhibition of KC activity. (**a**) Relationship between the phase of PN, LHI and KC spikes for different concentrations (σ = 0.2–0.4). Normalized phase histograms were computed using the phase of the PN, LHI and KC spikes with respect to the mean oscillatory membrane potential of the PNs during an odor presentation. The peak of the LFP oscillation corresponds to 0 radians; 0.09-radian bins. Normalization ensures that the area under the histogram is unity. Each concentric ring (dotted line) corresponds to a probability of 0.02. (**b**) Main peaks of the phase histograms in **a**. The phase difference between the excitatory PNs and the inhibitory LHIs decreased as a function of increasing concentration, ensuring that the KC spikes occurred in progressively smaller windows. (**c**) Average spike delay across all trials. The KC integration window, defined by the mean time delay (measured in terms of the phase of the PN LFP) of LHI spikes (shadowed area) decreased with decreasing s.d. Without inhibition, most KC spikes occurred outside this integration window. Discontinuous black lines show the mean time delay (dotted line) and the error bars (dashed lines) for KC spike timing in the absence of LHI inhibition. The solid black line shows the mean KC spike time delay in the presence of feedforward inhibition. (**d**) The phase distribution of LH and KC spikes for two concentrations (top, σ = 0.25; bottom, σ = 0.35). The peak phase of KC spikes in the absence of inhibition (right) occurred after the peak phase of LHI spikes. The magnitude of the peak KC phase increased dramatically with an increase in concentration. When LHI inhibition is present (left), most KC spikes that would have occurred after the peak of the LHI spike phase in the absence of inhibition were effectively cut off.

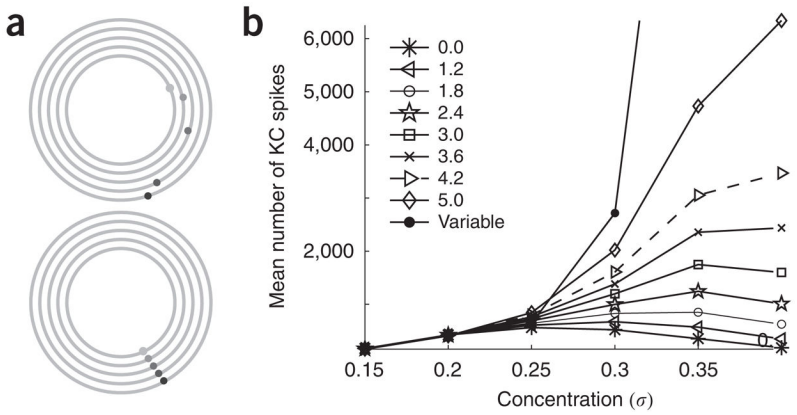

Figure 7.

Phase advance of LHIs maintains the sparseness of KC activity. (**a**) Top, the LHIs, on average, spiked at earlier phases of the oscillatory cycle as a function of increasing concentration. The filled circles show the peak LHI phase as a function of increasing concentration. Bottom, the effect of the phase advance on the response of KCs was demonstrated by introducing an increasing delay, $\Delta(\sigma)$, that offsets the LHI activity such that the mean phase of LHI spikes did not change as a function of increasing concentration. This disambiguates the effect of the amplitude of LHI activity from its phase advance. (**b**) The phase advance of LHI spiking activity modulated the KC response. Two extreme cases, corresponding to **a**, top (labeled '0.0'), and **a**, bottom (labeled 'variable'), show qualitatively different behavior for higher concentrations. The KC activity for intermediate fixed delays (Δ_0 = 1.2–5 ms) ranged between these two extremes.

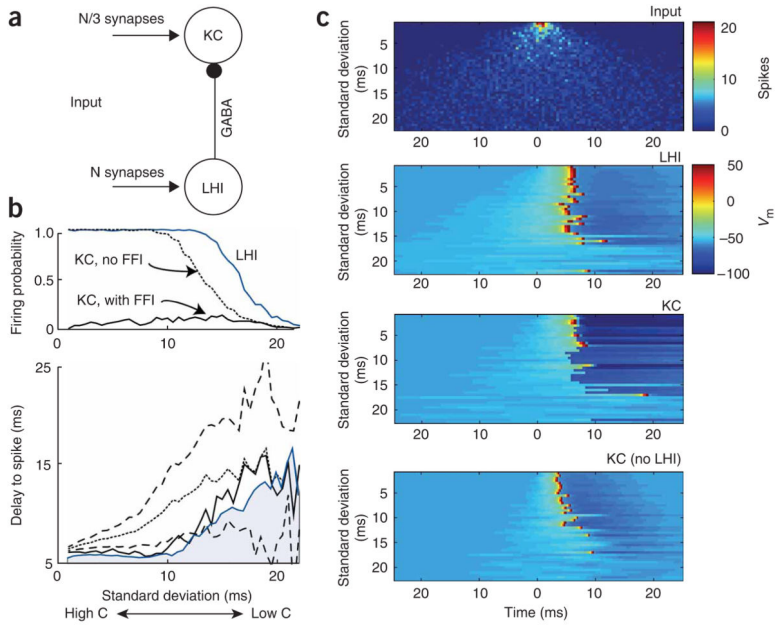

Figure 8.

Role of feedforward inhibition in a minimal neural circuit. (**a**) KC is inhibited by LHI. Both KC and LHI received normally distributed random depolarizing input emulating spikes from the antennal lobe. $N = 100$ synapses were connected to LHI. Of these, $N/3$ randomly selected synapses were connected to KC. (**b**) Top, probability of firing. The LHI spiking probability (solid blue line) increased with increasing coherence (decreasing s.d.), whereas the KC spiking probability (solid black line) remained low when it received feedforward inhibition from LHIs. In the absence of LHI inhibition, KC spiking probability (dotted black line) increased monotonically as a function of decreasing s.d. until it spiked reliably during each odor presentation. Bottom, average spike delay across all trials. The KC integration window, defined by the mean time delay of LHI spikes (light blue area), decreased with decreasing s.d. Without inhibition, most KC spikes occurred outside this integration window. Discontinuous black lines show the mean time delay (dotted line) and the error bars (dashed lines) for KC spike timing in the absence of LHI inhibition. The solid black line shows the mean KC spike time delay in the presence of feedforward inhibition. (**c**) External input and responses of KC and LHI for one representative trial of external stimulation. Top, arrival times (abcissa) of external spikes were plotted for different values of s.d. (ordinate). The color bar indicates number of input spikes in 0.5-ms bins. Middle, responses of LHI and KC in the presence of feedforward inhibition. Bottom, KC response in absence of LHI-mediated inhibition. The color bar indicates membrane voltage V_m.